Journal of the Iranian Chemical Society (2026) 23:193
https://doi.org/10.1007/s13738-026-03480-4

ORIGINAL PAPER

Molecular structure, spectral characteristics, and nonlinear optical properties of labetalol: an experimental and computational investigation

Mehmet Çınar[1] · **Sümeyra Can**[2]

Received: 2 April 2026 / Accepted: 19 May 2026 / Published online: 11 June 2026
© The Author(s) 2026

Abstract

Labetalol is an antihypertensive agent that possesses both α- and β-adrenergic blocking properties. This characteristic allows for its clinical use in both chronic hypertension and hypertensive emergencies. In this study, the FT-IR, FT-Raman, 1 H, 13 C, and DEPT-135 NMR spectra of labetalol hydrochloride (Labetalol HCl) were recorded and examined. Furthermore, the pharmacologically active (R, R) stereoisomer of labetalol was theoretically investigated using the B3LYP functional and the 6-311++G(d, p) basis set. The theoretically determined ground-state geometry of the molecule showed excellent agreement with experimental data reported in the literature. Using the obtained optimized structure, the vibrational spectra of the molecule were simulated, and the vibrational modes were assigned by evaluating them together with the experimental data. Nuclear Magnetic Resonance (NMR) analysis of the molecule was performed considering experimentally recorded values and calculations for gas phase, DMSO, and chloroform solvent environments, and the chemical shift values for each H and C atom were determined. Using Time-Dependent Density Functional Theory (TD-DFT) and Solvation Model based on Density (SMD) approaches, the UV-Vis spectra of the molecule were obtained in the gas phase and in four different solvent environments (ethanol, methanol, DMSO, and water). To better understand the electronic properties of the molecule, Frontier Molecular Orbitals (FMO), Molecular Electrostatic Potential Surface (MEPS), Hirshfeld surface analysis, Mulliken and Hirshfeld charge distributions, and Density States (DoS) analyses were performed. In addition, the non-linear optical (NLO) properties of the molecule were theoretically calculated, and the results showed that the molecule could be a promising NLO candidate.

Keywords Labetalol · B3LYP · DFT · Spectroscopy · Non-linear optics

Introduction

Hypertension, which occurs when blood pressure consistently stays above normal limits, is one of the leading health problems worldwide, leading to countless health complications and even death [1]. Today, a wide range of pharmacological agents are used to regulate and control blood pressure. These drugs are grouped according to their biological effects. Beta-blockers (β-adrenergic antagonists), which have been widely used in clinical practice for many years, are one of these groups. This class of antihypertensive drugs is an important treatment option, particularly recommended for patients with cardiovascular problems and those with additional risks such as diabetes, due to its effectiveness in controlling blood pressure [2, 3]. Labetalol is one of the drugs in the β-adrenergic antagonist group. With its complex

✉ Mehmet Çınar
prof.dr.mehmetcinar@gmail.com

Sümeyra Can
sumeyrasacakli@bayburt.edu.tr

[1] Technical Scientific Vocational School, Department of Electricity and Energy, Bayburt University, 69000 Bayburt, Turkey

[2] Health Services Vocational Schools, Department of Medical Services and Techniques, Bayburt University, 69000 Bayburt, Turkey

pharmacological structure, labetalol is described as the first representative of a group of drugs that block both α- and β-adrenoreceptors and are therefore used in antihypertensive treatment [4–7]. It acts as a competitive antagonist at α-adrenoreceptors, a non-selective competitive antagonist at β-adrenoreceptors, and has a postsynaptic effect [8, 9]. Labetalol also has a mechanism for blocking the effects of some endogenous chemicals on the heart and cardiovascular system. This blockage causes a decrease in heart rate and blood pressure. This reduces the workload on the heart and helps lessen the risk of heart failure [10]. In addition, in stressed patients, selective α-1 blockade of labetalol, in addition to non-selective beta-blockade, improves coronary hemodynamics and may have positive effects in myocardial ischemia. Selective α-1 blockade compounds have positive effects in preventing various types of arrhythmias [11].

Labetalol has four distinct stereoisomers due to the presence of two asymmetric centers in its structure. While the first two isomers, (S, S) and (R, S), are considered pharmacologically inactive, (S, R) and (R, R) (dilevalol) exhibit significant α-blocker and β-blocker effects. Labetalol, used in experimental and clinical studies, is a pharmacological formulation obtained by mixing these four stereoisomers in equal proportions [12–16]. Since non-specific drug toxicities develop independently of the chiral structure in most cases, this indicates that each enantiomer contributes to the resulting side effect to the same degree [15, 17, 18]. However, since labetalol is a well-tolerated β-blocker, side effects are generally mild and transient, occurring early in treatment [19].

The crystallographic structure of labetalol was first reported in 1984. This study revealed the solid-state structure and molecular conformation of the compound using X-ray diffraction [20]. Botes et al. investigated the salinization of five commercial beta-blockers, including labetalol, with nicotinic and isonicotinic acid using methanochemistry techniques [21]. Sanfilippo et al. reported the synthesis of active isomers of labetalol and structural verification of the products using NMR [22]. Absorption changes of labetalol and pseudoephedrine in the presence of β-cyclodextrin were investigated by UV-Vis analysis, and the resulting complexes were determined via absorption shifts [23]. Another study developed an RP-HPLC method that allows labetalol hydrochloride to be separated and determined without mixing with its oxidative degradation product, and supported experimental results by calculating molecule-stationary phase interactions and binding energies using DFT [24]. Carlo and Patrick analyzed the degradation mechanisms of five beta-blockers, including labetalol, using CID-MS/MS and supported the findings with DFT calculations [25]. Bernal et al. used quantitative structure-response relationship (QSAR) modeling and molecular dynamics simulations together to determine the biological activities and interaction profiles of new vasodilator candidates that can be used in the treatment of cardiovascular diseases [26]. They determined structural features such as HOMO energy, smoothness, and electronegativity and integrated computational modeling with experimental findings.

Based on the findings reported in the literature, this study aims to determine the ground-state structures of the monomeric and dimeric forms of the (R, R) stereoisomer of labetalol using the DFT/B3LYP method, to elucidate its molecular spectroscopic properties, and to compare them with the experimental spectroscopic characteristics of labetalol hydrochloride obtained from Fourier transform infrared (FT-IR), FT-Raman, ^{1}H, ^{13}C and DEPT-135 NMR analyses.

Materials and methods

Experimental studies

The Labetalol hydrochloride sample was procured from Apollo Scientific and used as received without further purification. FT-IR spectrum was recorded on a Perkin Elmer Spectrum One spectrometer in the 4000–400 cm^{-1} region at room temperature, employing a resolution of 4 cm^{-1} and 32 scans. FT-Raman measurements were carried out in the 4000–0 cm^{-1} region using a Thermo Scientific NXR FT-Raman module with a 1064 nm Nd: YAG laser as the excitation source. A liquid nitrogen-cooled germanium detector and a CaF_2 beam splitter were used in the spectrometer for spectral acquisition. NMR spectra were recorded at room temperature on a Bruker Avance III 400 MHz spectrometer with the compound dissolved in DMSO-d_6. Chemical shifts were reported in ppm relative to tetramethylsilane (TMS) as the internal standard for the ^{1}H and ^{13}C NMR spectra.

Computational methods

The ground-state equilibrium geometry of the molecule was completely optimized for an isolated system in the gas phase. Based on the optimized structure, vibrational frequency and NMR chemical shift calculations were carried out within the framework of density functional theory (DFT) [27, 28] at the B3LYP/6–311 + + G(d, p) level of theory [29, 30]. To improve agreement between calculated and experimental vibrational wavenumbers, scaling factors of 0.983 for frequencies below 1700 cm^{-1} and 0.958 for those above 1700 cm^{-1} were applied within the B3LYP method [31, 32]. Vibrational mode assignments were determined using potential energy distribution (PED) analysis implemented in the VEDA4 program [33]. The isotropic chemical shifts (^{1}H and ^{13}C NMR) were calculated using the

Gauge-Including Atomic Orbital (GIAO) method [34, 35], with tetramethylsilane (TMS) as the reference compound in both the gas phase and solvent phases (dimethyl sulfoxide -DMSO- and chloroform). UV–Vis spectral properties were determined using Time-dependent Density Functional Theory (TD-DFT) [36, 37] in both gas phase and four different solvent environments such as ethanol, methanol, water and DMSO. In the calculations, the Solvation Model based on Density (SMD) was preferred, which accounts for both electrostatic and non-electrostatic solvation effects by treating the solvent as a continuous dielectric medium, thereby providing theoretical spectra that are more consistent and reliable with experimental UV–Vis results in solution. The dipole moment, oscillator strengths, and absorption wavelengths were calculated for the first six electronically excited states, together with the HOMO–LUMO energies. Hirshfeld surface analysis was employed to elucidate intermolecular interactions in the crystal structure. In addition, Molecular Electrostatic Potential (MESP), Frontier Molecular Orbital (FMO), and Hirshfeld and Mulliken charge analyses were performed to evaluate the electronic charge distribution and the intra- and intermolecular interaction characteristics of the investigated molecule. Since the Density of States (DoS) plays an important role in understanding electronic structure and material properties, the corresponding DoS spectra were also analyzed. All structural parameters and spectroscopic properties were computed at the B3LYP/6–311 + + G(d, p) level using Gaussian 16 software [38]. Hirshfeld surface analysis was carried out using the available .cif file of the compound [21] with CrystalExplorer 3.1 [39], and DoS calculations were performed with GaussSum 3.0.2 [40] software.

Results and discussion

Molecular geometry

The crystallographic structure of (R, R)-Labetalol HCl was first described in the literature in 1984 [20]. Later, the salification of five beta blockers also including labetalol, with nicotinic and isonicotinic acid via mechanochemistry is described by Botes et al. [21]. To the best of our knowledge, these two studies are the only ones in the literature that have used experimental techniques to investigate the structure of labetalol, however, it should be emphasized that there are some differences between the data of these two studies. Therefore, the computational results from our study were compared with the two experimental studies mentioned. Since the ground-state structure of a molecule is used to calculate its spectroscopic properties in quantum-chemical computations, it is crucial to first identify the optimal ground-state structure. To optimize (R, R)-Labetalol, experimental data [21] were used as input parameters. For the isolated and monomeric (R, R)-Labetalol, the optimized geometrical structure is displayed in Fig. 1, whereas Fig. S1 shows the dimeric structure. Geometric parameters, including bond lengths, bond angles, and dihedral angles, are listed in Table 1 according to the atomic numbering in Fig. 1.

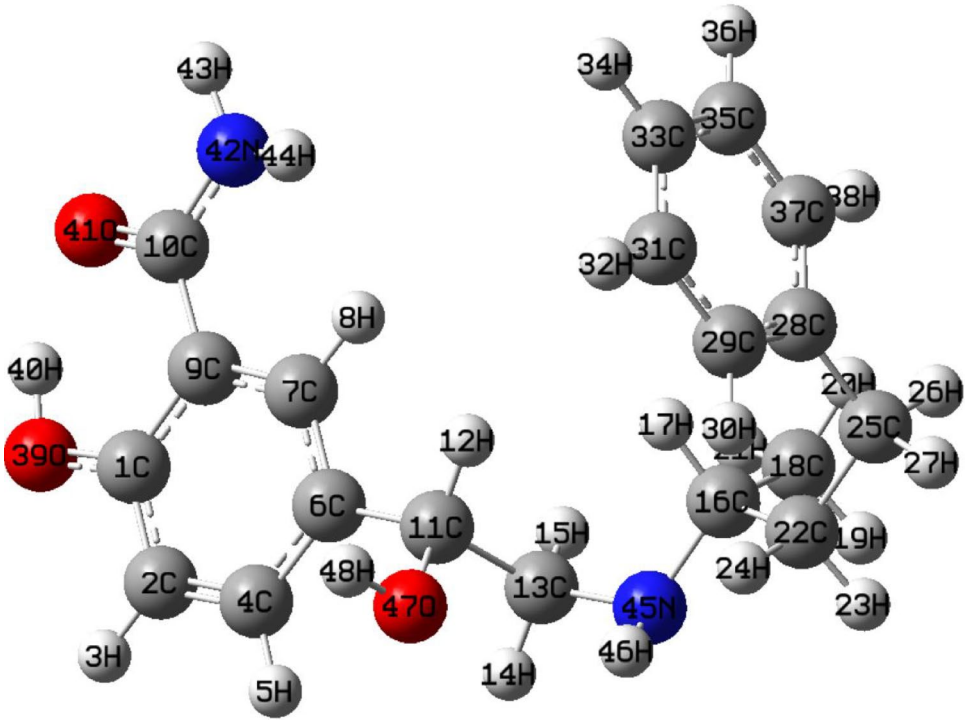

Fig. 1 Optimized equilibrium structure of (R, R)-labetalol (E = − 1073.984 Hartree = − 29224.62 eV) obtained by B3LYP/6-311 + + G(d, p)

Labetalol is a molecule that contains two aromatic rings—one with polar functional groups and the other a hydrophobic terminal phenyl ring—and single bonds between the aliphatic side chains, allowing for free rotation, thus exhibiting non-planar conformational flexibility. Therefore, (R, R)-Labetalol was investigated in this study, focusing on three fragments: the polar ring (ring 1), the hydrophobic ring (ring 2), and the aliphatic chain or backbone (Scheme 1).

When examining the polar ring, which is the first fragment for the monomer structure, the C-C bond lengths within the ring are calculated by B3LYP to be in the range of 1.381–1.417 Å. In the dimer structure, these bond lengths were found to be 1.389–1.438 Å, while experimental studies show these values to be in the range of 1.378–1.412 Å. Calculations for the ring-attached amide group also show a good correlation with experimental data; however, the C = O bond was estimated to be shorter, while the C-N bond was calculated to be longer. Experimental and theoretical studies showed that when examining the CCC bond angles in the ring, there are no significant deviations from the expected 120º angle. A similar situation occurs in the bond angles of the amide group, and a nearly planar angle was observed between the amide group and the ring. The predicted C-C bond lengths for the hydrophobic ring show very good agreement with the experimental data reported in [21] but reveal significant differences compared with the other experimental dataset [20]. These differences are valid for both experimental sets. The CCC bond angles of the ring were found to be exactly 120º in the study, while these angles were estimated with very small differences in the B3LYP calculations [21]. When examining the backbone connecting the two rings, it is observed, as expected, that the dimer calculations are closer to the experimental values than the monomer. The interatomic bond angles in the backbone can be estimated to be around 110º. The C-N-C bond angle is given as 118.4º in the study, and B3LYP's estimate is closer to this, as can be seen in Table 1 [21]. Overall, the B3LYP calculations are consistent with the experimental values, and appropriate optimization was performed to determine the spectroscopic properties. This can be seen in the r.m.s values given in the bottom row of Table 1. Our calculations are based on r.m.s. values are much more consistent with a study in the literature, and while this value is only 0.03 Å for bond lengths, it was found to be 1.69º for bond angles.

Vibrational (IR and Raman) analysis

The recorded FT-IR and FT-Raman spectra for labetalol hydrochloride, and simulated vibrational spectra for (R, R)-Labetalol are given in Figs. S2 and S3, respectively. The recorded wavelengths and calculated vibrational parameters, along with the assignments for each vibrational mode, are given in Table S1.

The (R, R)-Labetalol molecule consists of 48 atoms, and therefore 138 vibrational modes were calculated. Skeletal vibrations in organic molecules often come from the linear or branched chain structures within the molecule and fall between 1400 and 700 cm^{-1}. The pattern of the absorption bands typically changes significantly when a substituent is added to the chain or ring. These bands are so frequently referred to as "fingerprint" bands, and the appearance of this portion of the spectrum is often used to identify a molecule or structural unit. Group frequencies, on the other hand, are typically located much above or below the region where skeletal vibrations are found and, with a few exceptions, are mostly independent of the molecule's overall structure [41]. The distinctive region for quickly identifying C–H, O–H, and N–H stretching vibrations is the high-frequency range above 3000 cm^{-1} [42]. O-H stretching is identified by a very broad band seen about 3400–3600 cm^{-1}. However, hydrogen bonding between molecules in the condensed phase complicates the vibrational spectra. For the studied molecule, the stretching mode of the OH attached to the polar ring was estimated by B3LYP as a pure mode of 3830 cm^{-1}. For the OH stretching in the backbone, this value was calculated as 3175 cm^{-1} and recorded as 3177 cm^{-1} in the FT-IR. The O–H in-plane bending vibration occurs in the range of 1440–1395 cm^{-1}, while the O–H out-of-plane bending vibration appears in the 960–875 cm^{-1} region [43, 44]. The in-plane bending vibrations of both OHs were estimated at 1298 and 1406 cm^{-1}, and the recorded IR and Raman values of 1413 and 1418 cm^{-1} support these calculations. When we examined the out-of-plane OH bending modes, a pure vibration at 812 cm^{-1} and a contaminated vibration at 844 cm^{-1} were calculated for the ring-connected group. For the OH group located in the aliphatic chain, two contaminated vibrations were predicted at 306 and 329 cm^{-1}. Symmetric and asymmetric stretching vibrations of the amino group, as well as N–H stretching vibrations, are located in the region where O–H stretching bands are observed in the spectrum. The symmetric and asymmetric stretching modes of the NH_2 group, which belongs to the amide group, were calculated as pure vibrations at 3452 and 3733 cm^{-1}, respectively. The scissoring modes of NH_2 were calculated at 1581 and 1627 cm^{-1}, contaminated by other vibrational modes. The rocking mode of this group was predicted by B3LYP at 1057 and 1097 cm^{-1}, the twisting mode at 535 cm^{-1}, and the wagging mode at 235 and 240 cm^{-1}. The stretching mode of the N–H group in the aliphatic chain was calculated at 3382 cm^{-1}; in-plane bending vibrations were determined at 1494 and 1496 cm^{-1} and out-of-plane bending vibration at 725 cm^{-1}.

Table 1 Comparison of calculated and reported geometric parameters of Labetalol (monomer and dimer)

Bond lengths	Monomer	Dimer	Exp. 1[a]	Exp. 2[b]	Bond Lengths	Monomer	Dimer	Exp. 1[a]	Exp. 2[b]
C(1)-C(2)	1.404	1.390	1.399	1.386	C(7)-C(9)-C(10)	123.1	123.7	122.3	122.0
C(7)-C(9)	1.407	1.423	1.393	1.399	C(9)-C(10)-O(41)	121.5	122.9	120.6	120.1
C(9)-C(10)	1.483	1.443	1.502	1.487	C(2)-C(1)-O(39)	117.7	119.0	117.8	118.1
C(10)-O(41)	1.240	1.262	1.252	1.254	C(9)-C(10)-N(42)	119.0	119.0	120.2	119.2
C(10)-N(42)	1.361	1.391	1.331	1.330	O(41)-C(10)-N(42)	119.5	118.0	119.2	120.7
C(11)-C(13)	1.543	1.528	1.521	1.510	C(6)-C(11)-C(13)	112.3	108.0	111.2	110.1
C(11)-O(47)	1.437	1.424	1.427	1.342	C(6)-C(11)-O(47)	112.3	115.0	107.0	115.0
C(1)-C(9)	1.417	1.438	1.406	1.408	C(13)-C(11)-O(47)	105.4	106.4	111.3	111.8
C(13)-N(45)	1.457	1.520	1.495	1.494	C(9)-C(1)-O(39)	123.0	120.5	121.9	122.7
C(16)-C(18)	1.533	1.524	1.517	1.515	C(11)-C(13)-N(45)	115.3	114.6	111.9	113.5
C(16)-C(22)	1.537	1.537	1.460	1.523	C(18)-C(16)-C(22)	112.1	113.6	115.5	113.5
C(16)-N(45)	1.473	1.531	1.543	1.507	C(18)-C(16)-N(45)	109.8	110.2	107.8	110.1
C(6)-C(7)	1.387	1.389	1.410	1.383	C(22)-C(16)-N(45)	108.1	106.8	112.9	106.2
C(6)-C(11)	1.514	1.517	1.535	1.515	C(16)-C(22)-C(25)	115.7	114.2	114.0	113.9
C(22)-C(25)	1.543	1.546	1.398	1.527	C(1)-C(2)-C(4)	120.7	120.7	119.8	121.1
C(1)-O(39)	1.340	1.347	1.350	1.352	C(22)-C(25)-C(28)	114.5	113.5	110.6	110.2
C(25)-C(28)	1.516	1.514	1.659	1.603	C(25)-C(28)-C(29)	120.7	120.2	117.1	120.0
C(28)-C(29)	1.401	1.401	1.421	1.390	C(25)-C(28)-C(37)	121.3	121.4	125.0	119.9
C(28)-C(37)	1.399	1.398	1.397	1.390	C(29)-C(28)-C(37)	118.0	118.4	117.9	120.0
C(29)-C(31)	1.393	1.394	1.381	1.390	C(28)-C(29)-C(31)	121.1	120.1	119.6	120.0
C(31)-C(33)	1.395	1.392	1.396	1.390	C(29)-C(31)-C(33)	120.2	119.6	121.1	120.0
C(33)-C(35)	1.393	1.394	1.320	1.390	C(31)-C(33)-C(35)	119.4	120.1	119.7	120.0
C(35)-C(37)	1.395	1.393	1.425	1.390	C(33)-C(35)-C(37)	120.1	120.1	121.6	120.0
C(2)-C(4)	1.381	1.413	1.379	1.378	C(28)-C(37)-C(35)	121.1	121.0	119.6	120.0
C(4)-C(6)	1.408	1.401	1.412	1.392	C(2)-C(4)-C(6)	121.2	119.7	120.9	121.0
O….H		3.711			C(13)-N(45)-C(16)	116.8	120.5	113.6	118.4

Bond angles	Monomer	Dimer	Exp. 1	Exp. 2[b]	Dihedral angles	Monomer	Dimer	Exp. 1[a]	Exp. 2[b]
C(2)-C(1)-C(9)	119.3	120.5	120.3	119.2	C(37)-C(28)-C(29)-C(31)	0.4	0.6	7.3	0.0
C(4)-C(6)-C(7)	118.0	120.1	118.9	118.0	C(25)-C(28)-C(37)-C(35)	179.9	177.5	172.6	176.5
C(4)-C(6)-C(11)	121.0	119.6	120.5	121.5	C(29)-C(28)-C(37)-C(35)	-0.3	-0.9	-7.5	0.0
C(7)-C(6)-C(11)	121.0	120.2	120.5	120.5	C(28)-C(29)-C(31)-C(33)	-0.1	-0.1	-2.0	0.0
C(6)-C(7)-C(9)	122.5	121.8	120.3	122.4	C(29)-C(31)-C(33)-C(35)	-0.2	-0.6	-3.5	0.0
C(1)-C(9)-C(7)	118.4	117.2	119.7	118.4	C(31)-C(33)-C(35)-C(37)	0.2	0.3	3.5	0.0
C(1)-C(9)-C(10)	118.5	119.1	119.9	119.6	C(33)-C(35)-C(37)-C(28)	0.0	0.5	2.3	-0.0

Dihedral angles	Monomer	Dimer	Exp. 1[a]	Exp. 2[b]
C(1)-C(2)-C(4)-C(6)	0.1	-0.1	-1.5	0.6
C(2)-C(4)-C(6)-C(7)	0.7	0.8	2.7	0.5
C(2)-C(4)-C(6)-C(11)	-177.3	-174.6	178.9	-178.3
C(9)-C(1)-C(2)-C(4)	-1.1	-2.1	-0.3	-1.3
C(4)-C(6)-C(7)-C(9)	-0.5	0.7	-2.0	-0.7
C(11)-C(6)-C(7)-C(9)	177.5	176.2	178.2	178.0
C(4)-C(6)-C(11)-C(13)	72.4	99.4	47.6	114.8
C(4)-C(6)-C(11)-O(47)	-46.1	-142.0	-74.2	-12.6
C(7)-C(6)-C(11)-C(13)	-105.5	-76.0	-136.2	-63.9
C(7)-C(6)-C(11)-O(47)	135.9	42.5	102.0	168.7
C(6)-C(7)-C(9)-C(1)	-0.5	-2.8	0.2	0.0
C(6)-C(7)-C(9)-C(10)	179.0	177.6	177.7	179.0
C(1)-C(9)-C(10)-O(41)	-5.6	-5.0	-8.0	-5.9
C(1)-C(9)-C(10)-N(42)	175.1	177.1	172.3	173.3
C(7)-C(9)-C(10)-O(41)	174.9	174.6	174.3	173.1
C(7)-C(9)-C(10)-N(42)	-4.4	-3.4	-5.3	-7.7
O(39)-C(1)-C(2)-C(4)	179.3	178.7	179.8	169.0
C(6)-C(11)-C(13)-N(45)	178.3	164.3	170.5	161.9
O(47)-C(11)-C(13)-N(45)	-59.2	-71.8	-70.3	-32.7

Table 1 (continued)

Dihedral angles	Monomer	Dimer	Exp. 1[a]	Exp. 2[b]
C(2)-C(1)-C(9)-C(7)	1.3	3.5	1.0	1.0
C(11)-C(13)-N(45)-C(16)	-73.4	-64.9	-165.1	-60.3
C(2)-C(1)-C(9)-C(10)	-178.2	-177.0	-176.7	-179.9
O(39)-C(1)-C(9)-C(7)	-179.1	-177.3	-179.1	-179.3
C(18)-C(16)-C(22)-C(25)	65.5	74.8	-63.0	59.3
N(45)-C(16)-C(22)-C(25)	-173.4	-163.5	-61.7	-179.6
C(18)-C(16)-N(45)-C(13)	-78.3	-53.0	-76.1	-68.3
O(39)-C(1)-C(9)-C(10)	1.3	2.3	3.2	0.3
C(22)-C(16)-N(45)-C(13)	159.1	176.9	155.1	168.5
C(16)-C(22)-C(25)-C(28)	63.1	71.0	175.8	66.2
C(22)-C(25)-C(28)-C(29)	67.6	82.0	70.1	68.3
C(22)-C(25)-C(28)-C(37)	-112.6	-96.4	-109.8	-115.2
C(25)-C(28)-C(29)-C(31)	-179.9	-177.8	-172.8	-176.5

Bond lengths in Angstroms (Å), bond angles and dihedral angles in degrees (°). r.m.s. (bond lengths, Å); Monomer vs. Exp. 1: 0.05, Monomer vs. Exp. 2: 0.03, Dimer vs. Exp. 1: 0.05, Dimer vs. Exp. 2: 0.03. r.m.s. (bond angles, °); Monomer vs. Exp. 1: 2.40, Monomer vs. Exp. 2: 1.76, Dimer vs. Exp. 1: 2.80, Dimer vs. Exp. 2: 1.69. Exp. 1 data is taken from Ref. [20] and Exp. 2 data is taken from Ref. [21]

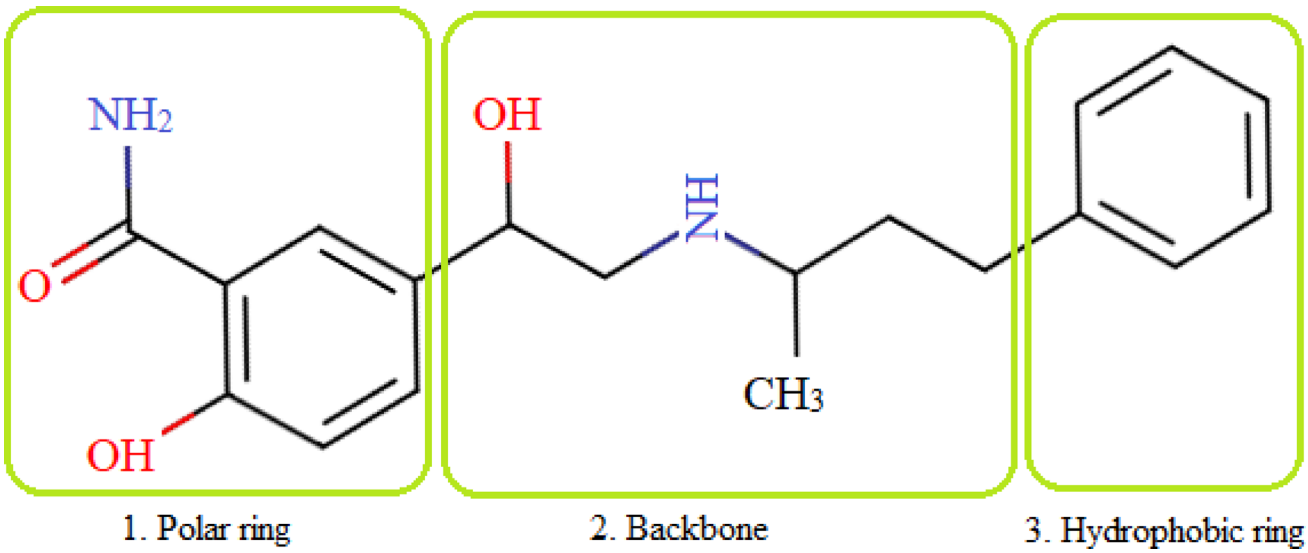

Scheme 1 Structure of labetalol

The C–H stretching vibration in the heteroaromatic structure appears in the 3000–3100 cm^{-1} region, which is characteristic for the rapid identification of aromatic C–H stretching vibrations [42]. On the other hand, -CH_3 group results in asymmetrical stretching frequency at 2940–2980 cm^{-1} and symmetrical C–H stretching absorption, which remains constant between 2850 and 2890 cm^{-1} [41]. The rings' CH stretching modes were calculated in the region of 3019–3062 cm^{-1}, and only one value at 3062 cm^{-1} is recorded in the experimental Raman spectrum within this region. Asymmetric stretching for the CH_2 and CH_3 groups in the backbone were calculated to be in the range of 2219–2967 cm^{-1}, while symmetric stretching modes were in the range of 2882–2907 cm^{-1}. The vibrational bands observed at 3812 and 3869 cm^{-1} are attributed to C–H stretching modes of the chiral centers along the molecular backbone. C–H in-plane bending vibrations are generally in the range of 1000–1300 cm^{-1}, while out-of-plane bending vibrations are approximately in the range of 650–1000 cm^{-1} [43, 44]. In the studied molecule, the in-plane C–H bending vibrations of the rings are distributed over the 1140–1500 cm^{-1} range; some are assigned as pure vibrational modes, whereas others are coupled with additional vibrational modes. The out-of-plane C–H bending vibrations appear in the 700–983 cm^{-1} region and, as shown in the table, most of them are assigned as pure modes. The scissoring modes of CH_2 and CH_3 groups located in the backbone correspond to the range of 1447–1482 cm^{-1}. At 1386 cm^{-1}, the CH_3 umbrella mode was identified as a pure mode. The wagging modes of these groups are in the range 1330–1372 cm^{-1}, while the twisting mode is indicated at 1070 and 1187 cm^{-1}. Since the C=O stretching vibration causes a significant change in the dipole

moment, a strong and distinct peak is obtained in the 1700–1800 cm^{-1} region [43, 45]. The vibrational mode recorded at 1673 and 1679 cm^{-1} in the FT-IR and Raman spectra, respectively, and calculated at 1670 cm^{-1}, was assigned as the C = O stretching. The spectral region of 1400–1650 cm^{-1}, located at the top of the fingerprint area, is the region where C = C stretching vibrations are observed, especially in aromatic rings. Five bands in this region at the intervals of 1625–1590, 1590–1575, 1540–1470, 1465–1430, and 1380–1280 cm^{-1} were identified [46].

The C–C stretching modes of the rings were recorded within a range consistent with the literature, and very good agreement was observed between experimental and calculated values in this region. For the two aromatic rings, the in-plane CCC bending vibrations were recorded and calculated to lie approximately in the 700–1100 cm^{-1} range. This region partially overlaps with the out-of-plane bending vibrations of the ring C–H bonds. Both vibration modes were calculated and recorded within the expected range and are consistent with the literature. Out-of-plane CCCC bendings are observed in a lower range, 700–400 cm^{-1}, and were calculated quite successfully by B3LYP in the 397–712 cm^{-1} range.

Nuclear magnetic resonance (NMR) analysis

The Gauge-Invariant Atomic Orbital (GIAO) method is formulated using an exponential multiplier that incorporates a vector potential in each atomic orbital, making it insensitive to gauge transformations of the magnetic field. It is currently the most widely accepted approach for calculating NMR spectra. In this context, the ^{1}H and ^{13}C NMR chemical shift values for the monomer and dimer (R, R)-Labetalol molecule were calculated using the GIAO method for different dielectric environments, including gas phase, chloroform, and dimethyl sulfoxide (DMSO) solvent, using the B3LYP hybrid functional and the 6-311 + + G(d, p) basis set. The ^{1}H, ^{13}C, and DEPT (Distortionless Enhancement by Polarization Transfer)-135 NMR spectra recorded in DMSO-d_6 are shown in Fig. S4. The recorded and calculated chemical shift values (ppm) for each H and C atom are given in Table 2. Proton and carbon chemical shift values for labetalol [22] and only proton chemical shift values for labetalol + isonicotinic acid [21] were previously recorded in DMSO solvent and published. In NMR spectra, especially 1H NMR spectra, it is very difficult to precisely assign chemical shifts to specific atoms. Therefore, the assignments in Table 2 take into account the studies mentioned above. Since the samples used in the experimental NMR spectrum consist of a mixture of (R, R) and (R, S) stereoisomers, many of the peaks in the ^{13}C NMR spectrum consist of two separate peaks very close to each other, each corresponding to a stereoisomer. Therefore, chemical shifts in carbon atoms can be more easily identified by also utilizing the DEPT-135 spectrum. In the DEPT-135 spectrum, positive peaks correspond to methine (CH) or methyl (CH_3) carbons, while negative peaks correspond to methylene (CH_2) carbons. On the other hand, quaternary carbons, which do not have protons, do not give a signal and are therefore not visible. Therefore, the methyl carbon is represented by the peak at 15.63 ppm, while the methylene carbons are represented by the peaks at 31.44, 33.77, and 50.65 ppm. Because oxygen is electronegative, the carbon atoms bonded to oxygen resonate in the downfield region. Both of the carbons to which the oxygen atoms are linked in this molecule showed a peak of 172.16 ppm. Similarly, the carbon atom to which the phenyl ring is attached to the backbone resonated in the downfield region, giving a chemical shift of 160.89 ppm. The carbon to which the amide group is linked produced a signal at 114.80 ppm, and the carbon to which the aliphatic chain is attached produced a signal at 141.36 ppm when the polar ring's carbon atoms without hydrogen bonds were examined. The signals at 68.32 and 53.79 ppm correspond to two backbone carbons: one is substituted with a hydroxyl group and a hydrogen, and the other with a methyl group and a hydrogen. Aromatic carbons are known to produce signals in the NMR spectrum with chemical shift values between 100 and 150 ppm [47–49].

The remaining carbons of the hydrophobic ring resonated in the range of 126.48-128.87 ppm. In the polar ring, two carbon atoms with equivalent chemical environments give rise to a signal at 132.20 ppm. In contrast, the remaining carbon, due to its different neighboring environment, resonates at 117.74 ppm. Even though monomeric and dimeric forms were handled independently in the computations, differences between the calculated model and the crystallographic structure impact the electronic structure and, consequently, the ensuing chemical shifts. Therefore, it is common to observe differences between the predicted and observed values. As can be seen from the r.m.s. values given in Table 2, the calculations for the monomeric structure are closer than those for the dimeric structure.

The signal at 12.95 ppm in the ^{1}H NMR spectrum shown in Fig. S4 was not predicted by theoretical calculations. The signal in question arises from the hydrogen-solvent interaction, since the experimental spectrum was recorded for Labetalol HCl, whereas the calculations were performed for the Labetalol molecule alone. It should also be emphasized that the signal observed at 3.39 ppm in the spectrum originates from water molecules and is not associated with the compound. Because the NH and OH protons in the compound under investigation can exhibit both intermolecular and solvent interactions, the largest discrepancies in the calculations are expected to arise from these protons.

Table 2 The recorded and predicted a. 1 H NMR isotropic chemical shifts (with respect to TMS, all values in ppm). b. 13 C NMR isotropic chemical shifts (with respect to TMS, all values in ppm)

Atom		Monomer			Dimer		
	Exp.	Gas	DMSO	Chloroform	Gas	DMSO	Chloroform
a. 1 H NMR isotropic chemical shifts (with respect to TMS, all values in ppm). b. 13 C NMR isotropic chemical shifts (with respect to TMS, all values in ppm)							
H(40)	9.34	12.40	12.24	12.28	13.11 / 13.12	12.74 / 12.74	12.73 / 12.74
H(5)	7.96	7.72	7.92	7.88	6.07 / 6.07	4.77 / 4.77	4.72 / 4.72
H(30)	7.44–7.47	7.58	7.89	7.80	7.33 / 7.33	7.75 / 7.75	7.54 / 7.54
H(32)	7.18–7.32	7.57	7.85	7.77	7.63 / 7.63	7.84 / 7.84	7.76 / 7.76
H(36)	7.18–7.32	7.46	7.77	7.67	7.94 / 7.94	7.83 / 7.82	7.88 / 7.87
H(38)	7.44–7.47	7.40	7.73	7.61	7.32 / 7.33	7.67 / 7.68	7.58 / 7.59
H(34)	7.18–7.32	7.39	7.68	7.59	7.77 / 7.77	7.69 / 7.69	7.75 / 7.75
H(3)	6.90	7.12	7.23	7.23	5.31 / 5.31	5.00 / 5.00	4.95 / 4.95
H(8)	7.96	6.71	7.45	7.19	5.75 / 5.75	5.20 / 5.20	5.09 / 5.09
H(44)	8.55–8.68	5.37	6.34	6.04	3.26 / 3.79	3.15 / 3.67	2.98 / 3.48
H(43)	8.55–8.68	4.60	5.35	5.17	3.26 / 3.79	3.14 / 3.68	2.98 / 3.48
H(12)	4.90	4.29	4.64	4.51	3.97 / 3.97	4.04 / 4.04	3.99 / 3.99
H(27)	2.69–2.81	3.00	3.10	3.08	2.65 / 2.96	2.83 / 3.01	2.77 / 2.97
H(14)	2.90–3.21	2.80	2.74	2.78	2.25 / 4.11	3.04 / 3.59	3.00 / 3.67
H(26)	2.69–2.81	2.59	2.81	2.73	2.65 / 2.96	2.83 / 3.01	2.77 / 2.97
H(15)	2.90–3.21	2.47	2.70	2.62	2.25 / 4.11	3.04 / 3.59	3.00 / 3.67
H(17)	2.69–2.81	2.56	2.65	2.60	4.43 / 4.42	3.91 / 3.90	4.12 / 4.11
H(24)	1.68–1.92	1.72	1.94	1.86	1.75 / 1.96	2.00 / 1.75	1.86 / 1.62
H(23)	1.68–1.92	1.76	1.69	1.74	1.75 / 1.96	2.00 / 1.75	1.86 / 1.62
H(46)	6.13	1.51	1.81	1.72	3.58 / 1.90	4.68 / 4.72	4.34 / 4.42
H(20)	1.34	1.20	1.46	1.34	2.53 / 2.53	2.07 / 2.07	2.25 / 2.25
H(21)	1.34	1.21	1.34	1.29	1.93 / 1.93	1.82 / 1.82	1.86 / 1.86
H(48)	1.06	0.49	0.95	1.10	2.65 / 2.65	2.59 / 2.60	2.95 / 2.95
H(19)	1.34	0.50	0.36	0.40	0.96 / 0.96	0.84 / 0.84	0.68 / 0.68
r.m.s.		1.42	1.37	1.58	2.03	1.94	2.02
b. 13C NMR isotropic chemical shifts (with respect to TMS, all values in ppm)							
C(10)	172.16	177.09	179.75	179.15	170.17 / 170.19	158.82 / 158.82	158.19 / 158.20
C(1)	172.16	172.79	171.58	171.85	173.98 / 173.98	170.30 / 170.30	170.32 / 170.32
C(28)	160.89	151.37	153.83	153.20	145.18 / 145.16	152.20 / 152.18	149.28 / 149.26
C(6)	141.36	140.55	143.32	142.65	137.37 / 137.37	144.57 / 144.57	142.92 / 142.92
C(4)	132.20, 132.53	139.54	140.82	140.61	107.89 / 107.85	103.84 / 103.84	103.56 / 103.55
C(37)	128.86, 128.87	136.32	137.51	137.03	135.85 / 135.86	137.38 / 137.40	137.12 / 137.14
C(31)	128.75, 128.77	135.19	136.10	135.83	135.93 / 135.92	135.98 / 135.97	135.81 / 135.81
C(29)	128.86,128.87	134.68	135.92	135.58	133.08 / 133.07	136.05 / 136.05	134.38 / 134.38
C(35)	128.75, 128.77	134.19	135.42	134.94	138.54 / 138.52	137.09 / 137.07	137.95 / 137.93
C(33)	126.48, 126.71	131.71	132.53	132.19	135.72 / 135.76	132.91 / 132.96	134.41 / 134.45
C(7)	132.20, 132.53	128.96	133.32	131.58	123.53 / 123.54	109.31 / 109.31	110.17 / 110.17
C(2)	117.74	126.19	124.64	125.36	109.08 / 109.07	105.27 / 105.27	105.23 / 105.22
C(9)	114.80	116.52	117.69	117.34	112.07 / 112.07	105.99 / 106.00	106.78 / 106.78
C(11)	68.32, 68.53	76.01	76.38	76.27	80.78 / 80.77	79.82 / 79.81	80.15 / 80.15
C(13)	50.65, 50.71	58.64	58.39	58.44	59.98 / 59.98	60.72 / 60.73	61.26 / 61.27
C(16)	53.79, 53.90	50.54	50.99	50.87	62.16 / 62.16	62.14 / 62.14	62.08 / 62.07
C(22)	33.77, 34.43	45.59	45.95	45.77	47.11 / 47.11	44.53 / 44.53	45.13 / 45.13
C(25)	31.44, 31.54	37.49	37.30	37.38	36.00 / 36.01	37.08 / 37.08	36.95 / 36.95
C(18)	15.63, 16.10	18.91	19.18	18.98	18.08 / 18.07	15.92 / 15.91	16.21 / 16.20
r.m.s.		6.37	6.48	6.22	11.79	11.62	9.80

The amino group protons appeared at 8.55–8.68 ppm in the experimental spectrum; however, the calculations, as expected, predict chemical shifts slightly upfield. A similar situation applies to the NH proton. For instance, this proton resonates at 6.13 ppm experimentally, while calculations predict a chemical shift of 1.51–1.81 ppm for the monomeric structure. In the dimeric structure, due to intermolecular interactions, this shift moves downfield. Therefore, it can be said that by aligning the theoretical framework more closely with the experimental one, B3LYP will be able to predict this value more accurately. The largest chemical shift in the spectrum (9.34 ppm) is attributed to the phenolic OH proton attached to the polar ring and is consistent with the literature in DMSO medium [50]. In contrast, theoretical GIAO calculations yield a value approximately 3 ppm larger (> 12 ppm), which is a common theoretical deviation for phenolic OHs. However, for the other OH proton in the aliphatic chain, this difference is quite small, particularly for the monomeric structure. This proton resonates at 1.06 ppm, a signal not reported in the literature. Protons in aromatic rings generally resonate in the range of 6.5–8.5 ppm. In benzene derivatives, such as simple phenyl groups, this range is 7.0–7.5 ppm, but these values can vary depending on the groups attached to the ring. For example, in aromatic rings containing electron-withdrawing groups, protons resonate at 7.5–8.5 ppm, while the chemical shift of protons shifts to the range of 6.5–7.2 ppm with the attachment of electron-donating groups [49, 51]. The five hydrogen atoms attached to the hydrophobic ring appeared in the range of 7.18–7.47 ppm. In the polar ring, the H(3) proton has a chemical shift of 6.90 ppm due to its distant interaction with the Oxygen atom, while the other two protons resonated at 7.96 ppm, consistent with the literature. While protons in the methyl group showed a chemical shift of 1.34 ppm, protons in the methylene groups, as expected, signaled with a higher shift, in the range of 1.68–3.21 ppm, the chemical shift values for protons located in chiral centers were recorded as 2.69–2.81 and 4.90 ppm, respectively. As with carbon atoms, calculations for protons in the monomer are more consistent with experimental values than for the dimer. The r.m.s value for the monomeric structure is 1.37 ppm when the calculations are performed in DMSO, but it is roughly 2.00 ppm for the dimeric structure. The discrepancies between experimental and calculated values are primarily due to the inability to perfectly replicate the experimental environment in calculations. Nevertheless, it can be said that DFT alone is sufficient for interpreting any NMR spectra and determining the molecular structure.

Analysis of electronic properties

To elucidate the electronic transitions of the investigated molecule, TD-DFT calculations of the electronic absorption spectrum were performed in vacuum and in four solvents: ethanol, methanol, water, and DMSO, considering six singlet → singlet spin-allowed excited states with the lowest energy. Simulated UV-Vis spectra of (R, R)-Labetalol for all media are given in Fig. 2. Furthermore, calculated values, including excitation energies, oscillator strengths (f), absorption wavelengths (λ), transition states, configuration interaction coefficients, and percentage contributions to electronic transitions, are presented in Table 3. The UV-Vis spectrum of Labetalol has been previously reported, with maximum absorption peaks at 302 nm [52] and 308 nm [53]. Compared to previous literature, a higher resolution UV-Vis spectrum was obtained; this spectrum revealed three maximum absorption peaks at wavelengths of 206, 232, and 302 nm [54]. As shown in Table 3, in this study, considering six singlets → singlet spin-allowed excited states with the lowest energy, only one electronic transition's oscillator strength was found to be non-zero for media other than ethanol. The second non-zero *f* value obtained for the ethanol solvent is quite small. Oscillator strength (*f*) measures how strongly a transition interacts with light, and if the dipole transition moment between two energy levels is zero, $f = 0$, meaning that the transition is optically forbidden. In this case, for (R, R)-Labetalol, a single allowed transition around 320 nm in the solvent medium was calculated, corresponding to a transition from the ground to the first excited state. When solvent effects are excluded (i.e., in a vacuum), this electronic transition was predicted to occur at 328.6 nm. Fig. S5 illustrates the frontier molecular orbital patterns that are crucial to electronic transitions. The energy values and energy differences of these molecular orbitals can be seen in Table 4. Other crucial parameters, such as ionization potential, electron affinity, chemical hardness and softness, electronegativity, electronic chemical potential, and the electrophilicity index—which is a measure of a molecule's overall propensity to accept electrons—can be calculated from the HOMO and LUMO energy values of a molecule or molecular system. The TD-DFT-calculated values for all these parameters are listed in Table 5. As can be seen from the frontier molecular orbital patterns and Table 3, the optically allowed only one transition occurs from HOMO to LUMO, and is assigned as $\pi \rightarrow \pi^*$. HOMO is localized to the relatively electron-rich π-conjugated regions of the molecule, while LUMO is distributed preferentially over electron-withdrawing functional groups that represent potential electron-accepting regions. This indicates intramolecular charge transfer from the donor to the acceptor. To estimate the atomic charge distribution, Mulliken population

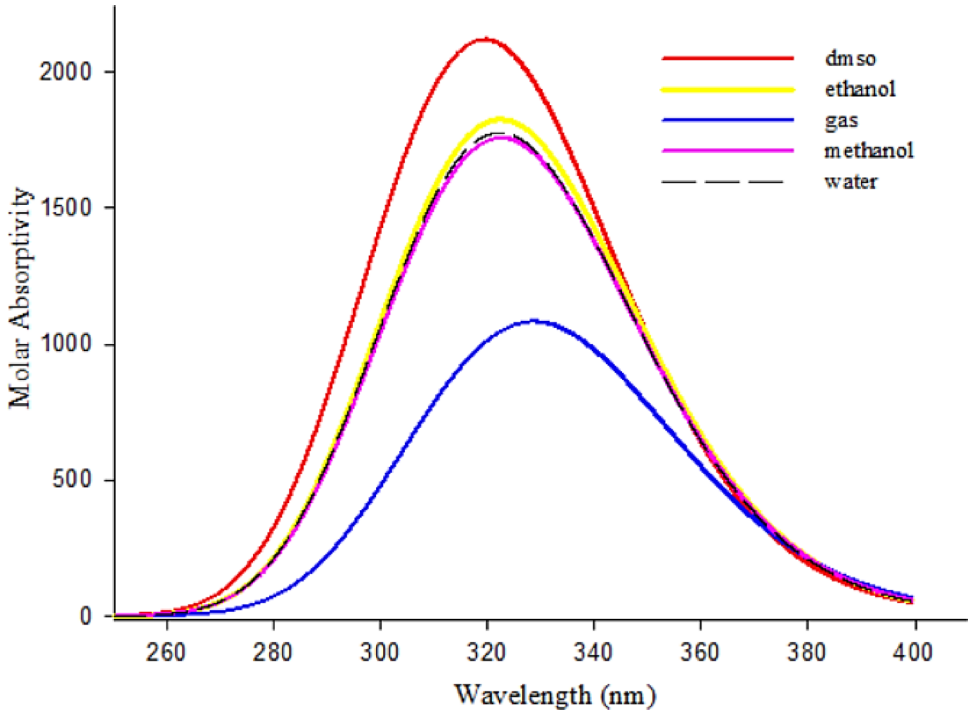

Fig. 2 Simulated UV-Vis spectra of (R, R) -labetalol

Table 3 Calculated absorption wavelengths (λ, nm), excitation energies (E, eV), oscillator strengths (f) and the highest electron transitions percentages (%) of the (R, R)-Labetalol in vacuum and solvents

Media	λ (nm)	E (eV)	*f*	Transition states	Coefficients	%
Gas	392.1	3.162	0	(88→89)	0.54966	30.21
	349.2	3.551	0	(84→89)	0.47616	22.67
	331.1	3.745	0	(86→91)	0.3597	12.94
	328.6	3.773	0.0267	(88→89)	0.70135	49.19
	308.6	4.017	0	(87→89)	0.54961	30.21
	297.4	4.169	0	(84→89)	0.47849	22.9
DMSO	382.19	3.244	0	(88→89)	0.55322	30.61
	345.37	3.59	0	(84→89)	0.47319	22.39
	327.7	3.784	0	(86→90)	0.36918	13.63
	319.4	3.881	0.0523	(88→89)	0.69844	48.78
	296.9	4.175	0	(87→89)	0.54934	30.18
	293.9	4.219	0	(84→89)	0.45742	20.92
Ethanol	383.7	3.231	0	(88→89)	0.5464	29.86
	345.9	3.584	0	(84→89)	0.48258	23.29
	327.8	3.782	0.0066	(86→90)	0.36551	13.36
	322.4	3.846	0.0451	(88→89)	0.69951	48.93
	300.2	4.13	0	(87→89)	0.55071	30.33
	294.2	4.214	0	(84→89)	0.46119	21.27
Methanol	383.7	3.231	0	(88→89)	0.54532	29.74
	346	3.583	0	(84→89)	0.486	23.62
	327.7	3.783	0	(86→90)	0.36392	13.24
	322.6	3.843	0.0434	(88→89)	0.69964	48.95
	300.5	4.125	0	(87→89)	0.54897	30.14
	294.2	4.214	0	(84→89)	0.45966	21.13
Water	383.5	3.233	0	(88→89)	0.5452	29.72
	345.9	3.585	0	(84→89)	0.48615	23.63
	327.6	3.785	0	(86→90)	0.36362	13.22
	322.2	3.848	0.0439	(88→89)	0.69952	48.93
	300	4.132	0	(87→89)	0.54857	30.09
	294.1	4.216	0	(84→89)	0.45885	21.06

Table 4 Energy values and energy differences of molecular orbitals playing an active role in electronic transitions calculated for the (R, R)-Labetalol, all values in eV

	Gas	DMSO	Ethanol	Methanol	Water
E_{HOMO}	-6.01	-5.91	-5.94	-5.95	-5.95
E_{HOMO-1}	-6.64	-6.52	-6.56	-6.58	-6.58
E_{LUMO}	-1.73	-1.49	-1.56	-1.57	-1.57
E_{LUMO+1}	-0.75	-0.45	-0.46	-0.45	-0.45
$\Delta E_{(LUMO+1)-HOMO}$	5.26	5.46	5.48	5.49	5.50
$\Delta E_{(LUMO+1)-(HUMO-1)}$	5.89	6.07	6.11	6.12	6.13
$\Delta E_{LUMO-HOMO}$	4.28	4.42	4.38	4.37	4.38
$\Delta E_{LUMO-(HOMO-1)}$	4.91	5.03	5.01	5.00	5.01

analysis [55] and the Hirshfeld partitioning scheme [56] were employed. The atomic charge distributions obtained using both methods are listed in Table S3. According to these results, Mulliken population analysis indicates a net charge transfer from the hydrophobic ring-chain fragment to the polar ring, supporting the donor-acceptor behavior highlighted above. On the other hand, Hirshfeld charges indicate negative charge accumulation on both aromatic rings and a mainly localized positive charge on the aliphatic chain. Mulliken analysis emphasizes directional charge transfer, while Hirshfeld analysis reflects a more balanced, delocalized electron density distribution [57]; thus, the two population analysis methods yield qualitatively different charge distributions.

The calculated energy values are very similar for ethanol, methanol, and water, while a slight shift is observed for DMSO, and the difference is more pronounced in the gas phase. The HOMO energy levels were predicted between − 5.91 and − 6.01 eV, while the LUMO levels ranged from − 1.49 to -1.73 eV, resulting in an energy gap of 4.28–4.42 eV. This indicates that (R, R)-Labetalol has a relatively wide energy gap, thus high electronic stability and a tendency to react independently of external factors (solvents), stemming solely from its own electronic structure, i.e., low intrinsic reactivity. In molecular systems, the ionization potential is directly related to the HOMO energy level, and the electron affinity to the LUMO energy level. The energy gap, defined as the difference between these two boundary orbitals, is one of the most critical measures of a structure's chemical stability. After determining the HOMO and LUMO energy values of a molecule, other fundamental parameters such as chemical hardness, softness, electronegativity, and electrophilic index, as well as electrical properties such as ionization potential ($I = -E_{HOMO}$) and electron affinity ($A = -E_{LUMO}$), can be calculated. These data, obtained within the framework of Koopmans' theorem [58] and theoretical approaches developed by Parr [59], allow for comprehensive analyses of the substance's reactivity, toxicity, aromatic character, and dynamic structure. Electron affinity refers to the energy change associated with the formation of a gaseous anion from a neutral atom. This quantity is physically observable and experimentally measurable. Systems with high A and I values are more prone to accepting new electrons rather than losing them. The ionization potential and electron affinity values indicate that the (R, R)-Labetalol molecule has a limited electron-donating ability and a moderate electron-accepting character.While the chemical hardness is relatively high, the softness values are low, supporting the molecule's chemically stable nature. Furthermore, the electrophilicity index indicates a moderately electrophilic character, consistent with partial intramolecular charge transfer rather than complete charge dissociation, as shown by the Hirshfeld charge distribution.

Another important tool frequently used to study intermolecular interactions in a molecular system and to determine the localization of nucleophilic and electrophilic attacks is the Molecular Electrostatic Potential (MESP) map. A color scale from red to dark blue characterizes the extreme negative and positive regions of the structure under study. A negative potential means that a proton will be attracted by that region, while a positive potential means that a proton will be repelled by that region. Green represents approximately the neutral region, while yellow represents a less negative region, and light blue represents a less positive

Table 5 The HOMO&LUMO energies and computed chemical reactivity parameters of (R, R)-Labetalol

Parameters	Formula	Gas	DMSO	Ethanol	Methanol	Water
LUMO energy (eV)	E_{LUMO}	-1.73	-1.49	-1.56	-1.57	-1.57
HOMO energy (eV)	E_{HOMO}	-6.01	-5.91	-5.94	-5.95	-5.95
Energy band gap	$\Delta E = E_{LUMO} - E_{HOMO}$	4.28	4.42	4.38	4.37	4.38
Ionization potential	$I = -E_{HOMO}$	6.01	5.91	5.94	5.95	5.95
Electron affinity	$A = -E_{LUMO}$	1.73	1.49	1.56	1.57	1.57
Chemical hardness	$\eta = (1 - A)/2$	2.14	2.21	2.19	2.19	2.19
Chemical softness	$\xi = 1/2\eta$	0.23	0.23	0.23	0.23	0.23
Electronegativity	$\chi = (1 + A)/2$	3.87	3.70	3.75	3.76	3.76
Chemical potential	$\mu = -(1 + A)/2$	-3.87	-3.70	-3.75	-3.76	-3.76
Electrophilicity index	$\psi = \mu^2/2\eta$	3.50	3.10	3.21	3.23	3.23

region. These maps also correlate with electron density and help predict from which direction a charged reactant (electrophile or nucleophile) will approach the molecule. The MAPS maps obtained for vacuum and four different solvents are presented in Fig. S6, and it can be seen that all maps were obtained similarly. The maps show that the negative electrostatic potential is concentrated on aromatic rings and heteroatom-containing functional groups, while the positive potential is predominantly localized in the aliphatic chain region. This distribution indicates that the electron density is concentrated on the rings and that the chain exhibits a relatively electron-deficient character, consistent with Hirshfeld analysis. It can also be said to visually support the trend of directional charge transfer predicted by Mulliken analysis. Therefore, it cannot be said that there is a complete charge dissociation within the molecule, but rather a partial and delocalized redistribution of intramolecular charge accompanied by donor-acceptor interactions.

The density of states (DoS) is the number of quantum states per unit volume at a given energy level in a system under thermal equilibrium and plays a key role in material kinetic theory. Total DoS (t-DoS) represents the total electronic density of states at each energy level as the sum of the contributions of all atoms and orbitals in a material, while partial DoS (p-DoS) refers to the portion of this total attributable to a specific atom, orbital, or spin component. The DoS spectrum of (R, R)-Labetalol was plotted by separating into three critical regions: the polar ring, the backbone (aliphatic chain), and the hydrophobic ring, and is given in Fig. 4. It should be kept in mind that the p-DoS spectrum is additive, with each fragment plotted by cumulatively adding its contribution to the previous ones. Therefore, the individual spectra of each fragment were plotted separately and are presented in Fig. S7. In the valence region between −20.0 and −6.0 eV, all three groups showed distinct peaks, with some peak positions overlapping in certain energy ranges. This indicates orbital hybridization between the groups. This hybridization shows that the molecule's electronic structure is shaped by multiple groups and that the valence-band electron distribution is complex. In the spectrum, the minimum point of the conduction band corresponds to the value where the binding energy is zero (E = 0), and the density of states approaching zero around −6.00 eV indicates a distinct HOMO–LUMO energy gap. The energy band gap of approximately 4.40 eV between the valence band peak and the conduction band bottom is consistent with the calculated energy gap. The contribution of the hydrophobic ring is significantly increased in the region near LUMO. Therefore, it can be said that the electronic character at the start of conduction is largely due to the hydrophobic ring.

Hirshfeld surface analysis

The Hirshfeld surface is a tool that divides the total electron density in a crystal structure into individual molecular parts, representing the spatial volume of the molecule within the crystal [60, 61]. Using this method, *van der Waals* contact distances are scanned to precisely determine intermolecular interaction points [56]. Hirshfeld surface analysis provides information about crystal packing by evaluating intermolecular contacts and interactions according to *van der Waals* radii.

After obtaining the Hirshfeld surface, the internal distance (d_i), the distance from a point on the surface to the nearest nucleus of the molecule in which that point is located, and the external distance (d_e), the distance from the same point on the surface to the nearest outer nucleus in a neighboring molecule, are also determined. The sum of these two values (d_i and d_e) gives the approximate *van der Waals* distance and indicates how close the atoms are to each other. Since d_i and d_e alone do not account for the atomic size, the normalized contact distance, d_{norm}, which allows for the identification of regions particularly important for intermolecular interactions, is obtained from the following formula, where r^{vdw} are the *van der Waals* radii of the atoms [62].

$$d_{norm} = \frac{d_i - r_i^{vdw}}{r_i^{vdw}} + \frac{d_e - r_e^{vdw}}{r_e^{vdw}}$$

If $d_{norm} < 0$ ($d_e < d_i$), the Hirshfeld surface is represented by red regions, indicating that the interatomic distances are shorter than the sum of the *van der Waals* radii. Therefore, strong and close-contact interactions, such as hydrogen bonds, are possible. If $d_{norm} > 0$ ($d_e > d_i$), the interatomic distances are greater than the sum of the van der Waals radii, and weak or negligible interactions are present. Blue regions on the Hirshfeld surface represent this situation. If $d_{norm} = 0$ ($d_e = d_i$), white regions correspond, where the interatomic distances are at the limit of the van der Waals radii and are in contact. Therefore, Hirshfeld surface analysis, when evaluated together with MEPS maps, can be used to investigate the electronic properties of the molecule. The Hirshfeld surface of Labetalol mapped onto d_{norm}, obtained from the *cif file from the [21] study, is shown in Fig. 3 (top). Surface examination reveals that the red regions are concentrated on the amide group, indicating OH interactions with neighboring molecules within the crystal structure or intermolecular interactions involving hydrogens bonded to nitrogen. The blue regions are mostly observed in aliphatic and hydrogen-rich regions and may represent weak or repulsive contacts. The remaining points visible on the surface correspond to H···H interactions. Previous assessments of charge transfer from Hirshfeld charge distribution and MEPS maps have

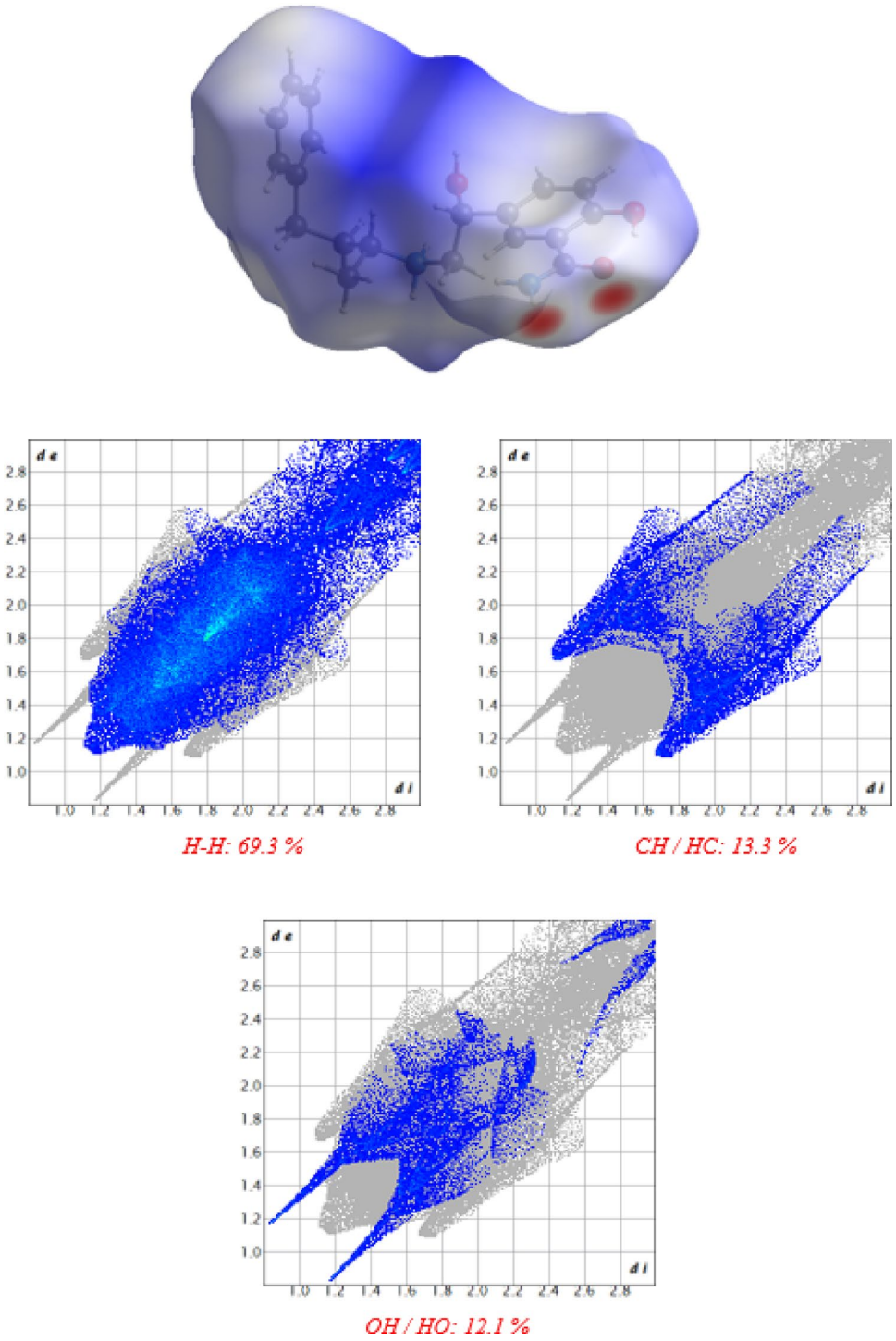

Fig. 3 The Hirshfeld surface (top) and the 2D fingerprint histogram for labetalol

been supported by the Hirshfeld surface, and a charge redistribution is reflected in the crystal packing. The bottom part of Fig. 3 presents the 2D fingerprint plot of the surfaces, displaying the partial contributions of the total surface and highlighting close intermolecular contacts, including H–H, O–H, and C–H. The two prominent spikes observed in the 2D fingerprint graphs correspond to characteristic O–H···O interactions, which cover 12.1% of the total surface. The distinctive 'wing' structures observed in Fig. 3 indicate C–H···π interactions; in this context, the contribution of C–H···C interactions to the total Hirshfeld surface is determined to be 13.3%. The calculations showed that H–H interactions are the dominant component of the Hirshfeld surface, accounting for 69.3% (see Fig. 4).

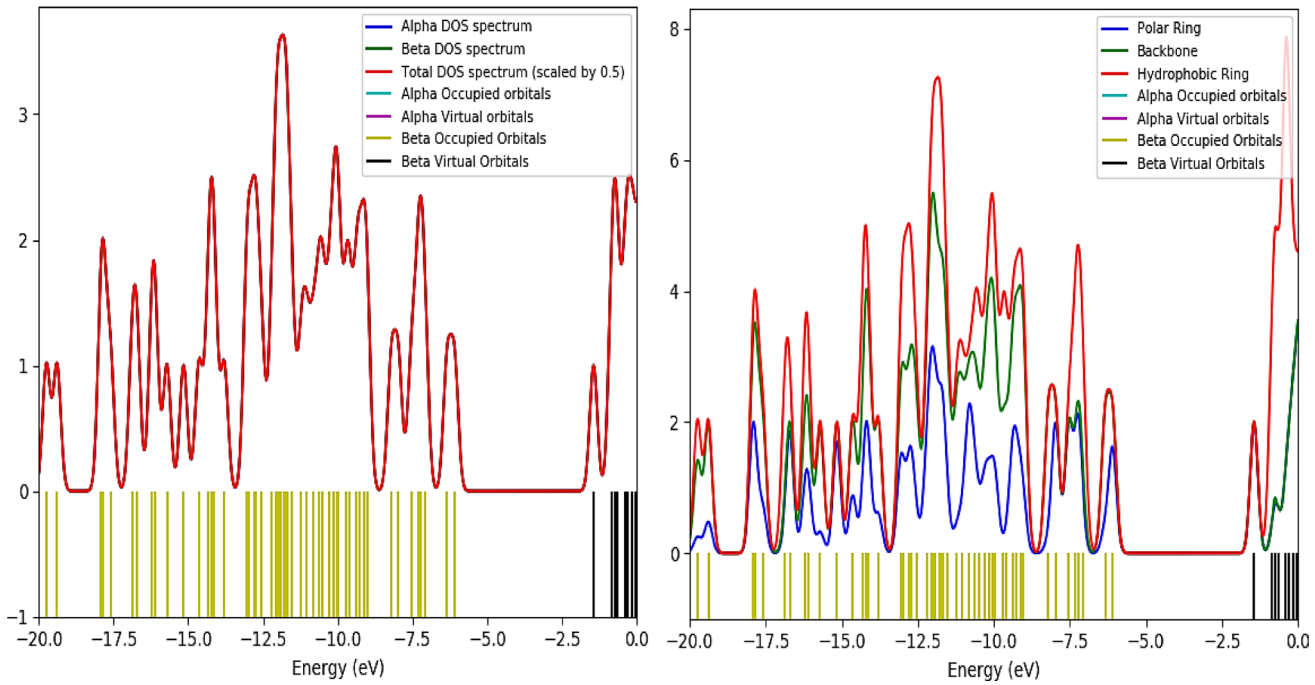

Fig. 4 t-DOS (left) and p-DOS (right) spectra of (R, R)-labetalol

Table 6 The electric dipole moment (μ, D), polarizability (α) and first hyperpolarizability (β) of (R, R)-Labetalol

	a.u.	esu (x 10^{-24})		a.u.	esu (x 10^{-30})
α_{xx}	225.852	33.468	β_{xxx}	-42.020	-0.363
α_{xy}	-30.933	-4.584	β_{xxy}	74.501	0.644
α_{yy}	272.427	40.370	β_{xyy}	-87.740	-0.758
α_{xz}	16.452	2.438	β_{yyy}	313.858	2.711
α_{yz}	-0.551	-0.082	β_{xxz}	-87.144	-0.753
α_{zz}	260.776	38.643	β_{xyz}	46.005	0.397
α_{tot}	253.018	37.493	β_{yyz}	126.712	1.095
$\Delta\alpha$	41.440	5.658	β_{xzz}	-111.822	-0.966
	a.u.	*Debye*	β_{yzz}	-3.502	-0.030
μ_x	0.000	0.000	β_{zzz}	150.667	1.302
μ_y	0.000	0.000	β_x	-241.581	-2.087
μ_z	1.810	4.602	β_y	384.857	3.325
μ_{tot}	1.810	4.602	β_z	190.235	1.643
			β_{tot}	492.611	4.256
			β_{vek}	190.235	1.643
			β_{vek}/β_{tot}	0.386	0.386

Non-linear optical (NLO) properties

Nonlinear optical (NLO) materials have been extensively studied owing to their important roles in various technologies, including optical communication, optical computing, data storage, optoelectronics, and photonic systems [63–65]. In this context, extensive studies are underway on molecules with nonzero hyperpolarization values that can serve as basic components of NLO materials.

To evaluate the NLO response of the investigated molecule, the total dipole moment (μ), mean polarizability (α), polarizability anisotropy (Δα), and first hyperpolarization (β) were calculated, and the results are presented in Table 6. The mathematical expressions and theoretical details used in the calculations are given in detail in our previous studies [31, 66]. The total dipole moment (μ_{tot}) is calculated to be 4.602 D, which is more than three times of the standard reference material urea (1.3732 D) [67]. On the other hand, the mean polarizability was found to be 37.493 × 10^{-24} esu is more than seven times greater than that of urea (5.0477 × 10^{-24} esu) [67]. This result can be attributed to the asymmetric charge distribution on the molecule. When the dipole moment values are examined, it is seen that the total dipole moment is only along the z-axis ($\mu_z = 4.602\ D$, $\mu_x = \mu_y = 0$). This indicates that the charge distribution within the molecule is not random, but rather correlated in a specific direction. In other words, one side of the molecule behaves as a relatively electron-rich character, while the other side behaves as an electron-poor character.

Hyperpolarizability (β) refers to a molecule's capacity to respond nonlinearly to an applied electric field. Therefore, it indicates the molecule's potential to alter the frequency of incident light or contribute to optical phenomena such as second-harmonic generation (SHG). A high β value suggests that the molecule may be significant for optoelectronic and photonic applications. The total first-order hyperpolarizability value calculated in this study ($\beta_{tot} = 4.256 \times 10^{-30}$ *esu*) is approximately 11 times greater than that of urea ($\beta \approx 0.372 \times 10^{-30}$ *esu*), which is used as a standard reference molecule in nonlinear optics (NLO) studies. This result

indicates that the molecule exhibits a more pronounced charge-transfer character and greater electronic delocalization under an electric field, and shows that the molecule is a promising candidate for NLO applications. However, the β_{vec}/β_{tot} ratio of 0.39 indicates that the molecule's nonlinear optical response is not perfectly aligned with the dipole moment direction. In other words, hyperpolarizability does not originate solely from the dipole moment direction; the β tensor components also have significant contributions in the *x* and *y* directions, as shown in Table 6. This suggests that the molecule does not possess a donor–π–acceptor architecture and that intramolecular charge transfer involves two-dimensional or multidirectional electron delocalization rather than occurring along a purely linear pathway. Consequently, while this molecule is theoretically a promising NLO candidate, the experimental SHG yield needs to be evaluated in conjunction with crystal structure analysis.

Conclusion

(R, R)-Labetalol, examined in this study, is one of the pharmacologically active stereoisomers of labetalol. However, while (R, R)-Labetalol was considered theoretically, experimental spectroscopic analyses were performed for Labetalol hydrochloride. This study aimed to determine the comprehensive ground-state geometry and spectroscopic properties of this compound, utilizing both experimental techniques and the strong predictive capabilities of DFT. The results obtained were evaluated comparatively using both experimentally recorded and theoretically calculated data; detailed comparisons were also made with studies reported in the literature. While it was not possible to fully replicate the crystallographic environment in the calculations, the optimized geometry showed very good agreement with the experimental crystal data. Indeed, as a result of the comparisons, r.m.s. values were calculated as 0.03 Å for bond lengths and 1.69° for bond angles. Both IR and Raman spectra of the compound were recorded and supported by theoretically simulated spectra. All data were evaluated together to assign vibrational modes, and characteristic vibrations critical for the identification of the compound were successfully determined. To improve the agreement between experimental and theoretical vibrational frequencies, the calculated raw frequencies were corrected with appropriate scaling coefficients, thus significantly improving the agreement between the two datasets. The recorded NMR spectra yielded results consistent with both previous studies and theoretical calculations. This clearly revealed the chemical shift values and bonding relationships of each carbon and hydrogen atom. Furthermore, a previously unreported signal of 1.06 ppm was observed in the ^{1}H NMR spectrum for Labetalol; this signal was determined to originate from a hydrogen bonded to an oxygen atom at one of the chiral centers in the aliphatic chain. UV–Vis spectra were obtained in different solvents to investigate the electronic properties of the molecule. The results revealed that the molecule did not exhibit strong interaction with solvents such as ethanol, methanol, water, and DMSO, and that the data obtained in solution were quite close to the values calculated for vacuum. Six electronic transitions were identified within the scope of TD-DFT calculations; five were found to be optically forbidden, with oscillator strengths close to zero. The only allowed transition was determined to occur at approximately 4.4 eV from HOMO to LUMO and to have π→π* character. The charge distribution of the molecule was investigated using both theoretical MESP analysis and Hirshfeld surface analysis based on crystallographic data. In addition, Mulliken and Hirshfeld atomic charge analyses were performed, and the two methods yielded slightly different results. When evaluated together with frontier molecular orbital analyses, Mulliken population analysis indicated a directional donor-acceptor-type charge transfer within the molecule, while Hirshfeld analysis showed that this process occurred as a partial, delocalized charge redistribution rather than a complete charge dissociation. Finally, the NLO properties of the molecule were examined, and it was determined that it has approximately 11 times higher hyperpolarizability values when compared to the reference substance, urea. This result suggests that the compound may be a promising NLO candidate; however, the experimental SHG yield should be evaluated alongside crystal structure analysis.

Supplementary Information The online version contains supplementary material available at https://doi.org/10.1007/s13738-026-03480-4.

Acknowledgements The computational analyses carried out in this study were performed using the TRUBA (Turkish National Science e-Infrastructure) resources provided by TUBITAK ULAKBIM. We would like to thank them for their computational infrastructure and technical support.

Author contributions Mehmet ÇINAR: Review & Editing, Software, Visualization, Conceptualization, Writing, Original Draft, Investigation, Data Curation. Sümeyra CAN: Writing, Review & Editing, Conceptualization, Software.

Funding Open access funding provided by the Scientific and Technological Research Council of Türkiye (TÜBİTAK). The authors declare that no funds, grants, or other support were received during the preparation of this manuscript.

Data availability Data will be made available on request.

Declarations

Conflict of interest The authors declare that they have no known competing financial interests or personal relationships that could have appeared to influence the work reported in this paper.

Open Access This article is licensed under a Creative Commons Attribution 4.0 International License, which permits use, sharing, adaptation, distribution and reproduction in any medium or format, as long as you give appropriate credit to the original author(s) and the source, provide a link to the Creative Commons licence, and indicate if changes were made. The images or other third party material in this article are included in the article's Creative Commons licence, unless indicated otherwise in a credit line to the material. If material is not included in the article's Creative Commons licence and your intended use is not permitted by statutory regulation or exceeds the permitted use, you will need to obtain permission directly from the copyright holder. To view a copy of this licence, visit http://creativecommons.org/licenses/by/4.0/.

References

1. B. Williams, The year in hypertension. J. Am. Coll. Cardiol. **55**(1), 65–73 (2009). https://doi.org/10.1016/j.jacc.2009.08.037
2. M.A. Ciciliati, de J.H.F. Jesus, É.T.G. Cavalheiro, Investigation of the thermal behavior of labetalol. Thermochim. Acta. **668**, 33–39 (2018). https://doi.org/10.1016/j.tca.2018.08.002
3. D. Kernaghan, G. McKay, Labetalol. Pract. Diabetes Int. **28**(3), 139–140 (2011). https://doi.org/10.1002/pdi.1579
4. J.B. Farmer, I. Kennedy, G.P. Levy, R.J. Marshall, Pharmacology of AH 5158; a drug which blocks both α- and β-adrenoceptors. Br. J. Pharmacol. **45**(4), 660–675 (1972). https://doi.org/10.1111/j.1476-5381.1972.tb08125.x
5. B. Jarrott, W.J. Louis, R.J. Summers, [3H]-guanfacine: a radioligand that selectively labels high affinity alpha2-adrenoceptor sites in homogenates of rat brain. Br. J. Pharmacol. **75**(2), 401–408 (1982). https://doi.org/10.1111/j.1476-5381.1982.tb08801.x
6. R.T. Brittain, G.P. Levy, A review of the animal pharmacology of labetalol, a combined alpha- and beta-adrenoceptor-blocking drug. Br. J. Clin. Pharmacol. **3**(4 Suppl 3), 681–684 (1976)
7. J. Mehta, J.N. Cohn, Hemodynamic effects of labetalol, an alpha- and beta-adrenergic blocking agent, hypertensive subjects. Circulation. **55**(2), 370–375 (1977). https://doi.org/10.1161/01.CIR.55.2.370
8. E.P. MacCarthy, S.S. Bloomfield, labetalol: a review of its pharmacology, pharmacokinetics, clinical uses and adverse effects. Pharmacotherapy. **3**(4), 193–219 (1983). https://doi.org/10.1002/j.1875-9114.1983.tb03252.x
9. A. Abdullah, M.K.M. Yusof, Labetalol: a brief current review. Pharmacophore. **10**(6), 50–56 (2019)
10. P.H.C. Yuen, C.R. Taddei, B.E. Wyka, I.A. Chaudry, Compatibility and stability of labetalol hydrochloride in commonly used intravenous solutions. Am. J. Hosp. Pharm. **40**(6), 1007–1009 (1983)
11. J.H. Kanto, Labetalol in the treatment of angina pectoris. Int. J. Clin. Pharmacol. Therapy Toxicol. **25**(3), 166–174 (1987)
12. J.E. Clifton, I. Collins, P. Hallett, D. Hartley, L.H.C. Lunts, P.D. Wicks, Arylethanolamines derived from salicylamide with alpha- and beta-adrenoceptor blocking activities. Preparation of labetalol, its enantiomers, and related salicylamides. J. Med. Chem. **25**(6), 670–679 (1982). https://doi.org/10.1021/jm00348a013
13. R.T. Brittain, G.M. Drew, G.P. Levy, The α- and β-adrenoceptor blocking potencies of labetalol and its individual stereoisomers in anaesthetized dogs and in isolated tissues. Br. J. Pharmacol. **77**(1), 105–114 (1982). https://doi.org/10.1111/j.1476-5381.1982.tb09275.x
14. T. Baum, R.W. Watkins, E.J. Sybertz, S. Vemulapalli, K.K. Pula, E. Eynon, S. Nelson, G.V. Vliet, J. Glennon, R.M. Moran, Antihypertensive and hemodynamic actions of SCH 19927, the R, R-isomer and labetalol. J. Pharmacol. Exp. Ther. **218**(2), 444–452 (1981)
15. P. Chrisp, K.L. Goa, Dilevalol: A review of its pharmacodynamic and pharmacokinetic properties, and therapeutic potential in hypertension. Drugs. **39**(2), 234–263 (1990)
16. E.J. Sybertz, C.S. Sabin, K.K. Pula, G.V. Vliet, J. Glennon, E.H. Gold, T. Baum, Alpha and beta adrenoceptor blocking properties of labetalol and its R, R-isomer, SCH 19927. J. Pharmacol. Exp. Ther. **218**(2), 435–443 (1981)
17. B.J. Materson, N.D. Vlachakis, S.P. Glasser, C. Lucas, K.B. Ramanathan, S. Ahmad et al., Influence of beta2 agonism and beta1 and beta2 antagonism on adverse effects and plasma lipoproteins: Results of a multicenter comparison of dilevalol and metoprolol. Am. J. Cardiol. **63**(19 Suppl), I58–I63 (1989)
18. J.A. Schoenberger, W.H. Frishman, J.D. Wallin, J. Gorwit, M.E. Davidov, E.L. Michelson et al., Dilevalol compared with propranolol and placebo for systemic hypertension. Am. J. Cardiol. **63**(19 Suppl), I45–I49 (1989)
19. A. Korzets, P. Danby, M.E. Edmunds, J. Feehally, J. Walls, Acute renal failure associated with a labetalol overdose. Postgrad. Med. J. **66**(771), 66–67 (1990). https://doi.org/10.1136/pgmj.66.771.66
20. P. Murray-Rust, J. Murray-Rust, D. Hartley, P. Hallett, J. Clifton, (R,R)-labetalol hydrochloride: determination of the absolute configuration of the high-melting polymorph, C19H25N2O3+·Cl–. Acta Crystallogr. Sect. C Cryst. Struct. Commun. **40**(5), 828–830 (1984). https://doi.org/10.1107/S0108270184005874
21. D.S. Botes, J.D. Loya, M. Ghahremani, B.B. Newham, M.I. Aleman, G.C. George, I.I.I. Unruh, D. K., K.M. Hutchins, Efficient mechanochemistry of beta blockers: neutralization, salification, and effect of liquid additives. RSC Mechanochem. **1**(5), 492–503 (2024). https://doi.org/10.1039/D4MR00078A
22. C. Sanfilippo, A.A. Paternò, A. Patti, Resolution of racemic amines via lipase-catalyzed benzoylation: chemoenzymatic synthesis of the pharmacologically active isomers of labetalol. Mol. Catal. **449**, 79–84 (2018). https://doi.org/10.1016/j.mcat.2018.02.017
23. A.A.M. Prabhu, N. Rajendiran, Encapsulation of labetalol, pseudoephedrine in β-cyclodextrin cavity: spectral and molecular modeling studies. J. Fluoresc. **22**(6), 1461–1474 (2012). https://doi.org/10.1007/s10895-012-1083-8
24. K.A. Attia, N.M. El-Abassawi, R.A. Said, A. El-Olemy, S. Ramzy, Computational investigation for practical HPLC determination of labetalol hydrochloride. Anal. Chem. Lett. **6**(6), 697–705 (2016)
25. M.J. Carlo, A.L. Patrick, Further exploration of the collision-induced dissociation of select beta blockers: acebutolol, atenolol, bisoprolol, carteolol, and labetalol. J. Mass Spectrom. **58**(12), e4985 (2023). https://doi.org/10.1002/jms.4985
26. A. Bernal, E.A. Márquez, M. Flores-Sumoza, S.A. Cuesta, J.R. Mora, J.L. Paz, D.C. Carrascal-Hernández, Molecular modeling of vasodilatory activity: unveiling novel candidates through density functional theory, QSAR, and molecular dynamics. Int. J. Mol. Sci. **25**(23), 12649 (2024)
27. P. Hohenberg, W. Kohn, Inhomogeneous electron gas. Phys. Rev. **136**(3B), B864–B871 (1964). https://doi.org/10.1103/PhysRev.136.B864
28. W. Kohn, L.J. Sham, Self-consistent equations including exchange and correlation effects. Phys. Rev. **140**(4A), A1133–A1138 (1965). https://doi.org/10.1103/PhysRev.140.A1133

29. A.D. Becke, A new mixing of Hartree–Fock and local density-functional theories. J. Chem. Phys. **98**(2), 1372–1377 (1993). https://doi.org/10.1063/1.464304
30. A.D. Becke, Density-functional thermochemistry. III. The role of exact exchange. J. Chem. Phys. **98**(7), 5648–5652 (1993). https://doi.org/10.1063/1.464913
31. M. Cinar, N. Yildiz, M. Karabacak, M. Kurt, Determination of structural, spectrometric and nonlinear optical features of 2-(4-hydroxyphenylazo) benzoic acid by experimental techniques and quantum chemical calculations. Spectrochim. Acta Part A Mol. Biomol. Spectrosc. **105**, 80–87 (2013)
32. M. Cinar, S. Can, Ö. Baris, Ç.E. Demirci, Diltiazem and verapamil: combined experimental and computational approaches to structural and spectroscopic characterization. J. Mol. Struct. **1295**, 136712 (2024)
33. M.H. Jamróz, *Vibrational Energy Distribution Analysis (VEDA 4) [Computer software]* (Warsaw, Poland, 2004)
34. R. Ditchfield, Molecular orbital theory of magnetic shielding and magnetic susceptibility. J. Chem. Phys. **56**(11), 5688–5691 (1972). https://doi.org/10.1063/1.1677088
35. K. Wolinski, J.F. Hinton, P. Pulay, Efficient implementation of the gauge-independent atomic orbital method for NMR chemical shift calculations. J. Am. Chem. Soc. **112**(23), 8251–8260 (1990). https://doi.org/10.1021/ja00179a005
36. E. Runge, E.K.U. Gross, Density-functional theory for time-dependent systems. Phys. Rev. Lett. **52**(12), 997 (1984). https://doi.org/10.1103/PhysRevLett.52.997
37. M.E. Casida, Time-dependent density-functional theory for molecules and molecular solids. in *Recent Advances in Density Functional Methods Part I* ed. by D.P. Chong (1995), p. 155–192. https://doi.org/10.1142/2914
38. M.J. Frisch, G.W. Trucks, H.B. Schlegel et al., *Gaussian 16 (Revision C.01) [Computer software]* (Gaussian, Inc., 2016)
39. M.J. Turner, J.J. McKinnon, S.K. Wolff, D.J. Grimwood, P.R. Spackman, D. Jayatilaka, M.A. Spackman, *CrystalExplorer17 [Computer Software]* (University of Western Australia, 2017)
40. N.M. O'Boyle, A.L. Tenderholt, K.M. Langner, cclib: A library for package-independent computational chemistry algorithms. J. Comput. Chem. **29**(5), 839–845 (2008). https://doi.org/10.1002/jcc.20823
41. C.N. Banwell, E.M. McCash, in *Fundamentals of Molecular Spectroscopy*. (Indian ed., 2017)
42. R.M. Silverstein, G.C. Bassler, T.C. Morrill, *Spectrometric Identification of Organic Compounds* (Wiley, 1991)
43. R.M. Silverstein, G.C. Bassler, Spectrometric identification of organic compounds. J. Chem. Educ. **39**(11), 546 (1962)
44. G. Socrates, *Infrared and Raman Characteristic Group Frequencies: Tables and Charts* (Wiley, 2004)
45. B.H. Stuart, *Infrared Spectroscopy: Fundamentals and Applications* (Wiley, 2004)
46. G. Varsanyi, *Assignments of Vibrational Spectra of 700 Benzene Derivatives* (Wiley, 1974)
47. H.-O. Kalinowski, S. Berger, S. Braun, L. Griffiths, Carbon-13 NMR spectroscopy. Anal. Chim. Acta. **221**, 367–368 (1989)
48. K. Pihlaja, E. Kleinpeter, *Carbon-13 NMR Chemical Shifts in Structural and Stereochemical Analysis* (Wiley-VCH, 1994)
49. L. Morsch, S. Farmer, K. Cunningham, Z. Sharrett, K.M. Shea, (2023). Organic chemistry II [open educational resource textbook]. Smith College. https://scholarworks.smith.edu/textbooks/6
50. P. Charisiadis, V.G. Kontogianni, C.G. Tsiafoulis, A.G. Tzakos, M. Siskos, I.P. Gerothanassis, 1H-NMR as a structural and analytical tool of intra- and intermolecular hydrogen bonds of phenol-containing natural products and model compounds. Molecules. **19**(9), 13643–13682 (2014). https://doi.org/10.3390/molecules190913643
51. M. Balci, *Basic 1H- and 13 C-NMR Spectroscopy* (Elsevier, 2005)
52. E.G. Clarke C. (ed.), *Isolation and Identification of Drugs*, vol 1 (Pharmaceutical, London, 1969), p. 255–234
53. J. Krzek, A. Kwiecień, Application of densitometry for determination of beta-adrenergic-blocking agents in pharmaceutical preparations. JPC J. Planar Chromatogr. Mod. TLC **18**(4), 308–313 (2005)
54. SIELC Technologies, (2026). UV-vis spectrum of labetalol. https://sielc.com/uv-vis-spectrum-of-labetalol
55. R.S. Mulliken, Electronic population analysis on LCAO–MO molecular wave functions. I J. Chem. Phys. **23**(10), 1833–1840 (1955). https://doi.org/10.1063/1.1740588
56. F.L. Hirshfeld, Bonded-atom fragments for describing molecular charge densities. Theoret. Chim. Acta. **44**(2), 129–138 (1977). https://doi.org/10.1007/BF00549096
57. F. Martin, H. Zipse, Charge distribution in the water molecule—a comparison of methods. J. Comput. Chem. **26**(1), 97–105 (2005). https://doi.org/10.1002/jcc.20157
58. A. Szabo, N.S. Ostlund, *Modern Quantum Chemistry: Introduction to Advanced Electronic Structure Theory* (Dover, 1996)
59. R.G. Parr, L.V. Szentpály, S. Liu, Electrophilicity index. J. Am. Chem. Soc. **121**(9), 1922–1924 (1999). https://doi.org/10.1021/ja983494x
60. M.A. Spackman, P.G. Byrom, A novel definition of a molecule in a crystal. Chem. Phys. Lett. **267**(3–4), 215–220 (1997). https://doi.org/10.1016/S0009-2614(97)00100-0
61. M.A. Spackman, D. Jayatilaka, Hirshfeld surface analysis. CrystEngComm. **11**(1), 19–32 (2009). https://doi.org/10.1039/B818330A
62. M.A. Spackman, J.J. McKinnon, Fingerprinting intermolecular interactions in molecular crystals. CrystEngComm. **4**(66), 378–392 (2002). https://doi.org/10.1039/B203191
63. J. Zyss, Molecular nonlinear optics: materials, phenomena and devices-Preface. Chem. Phys. **245**(1–3), VII–IX (1999)
64. S.P. Karna, Electronics and optical materials. J. Phys. Chem. A **104** (2000)
65. D.R. Kanis, M.A. Ratner, T.J. Marks, Design and construction of molecular assemblies with large second-order optical nonlinearities. Quantum chemical aspects. Chem. Rev. **94**(1), 195–242 (1994)
66. M. Cinar, A. Coruh, M. Karabacak, FT-IR, UV–vis, 1H and 13 C NMR spectra and the equilibrium structure of organic dye molecule disperse red 1 acrylate: a combined experimental and theoretical analysis. Spectrochim. Acta Part A Mol. Biomol. Spectrosc. **83**(1), 561–569 (2011)
67. S. Gatfaoui, N. Issaoui, T. Roisnel, H. Marouani, Synthesis, experimental and computational study of a non-centrosymmetric material 3-methylbenzylammonium trioxonitrate. J. Mol. Struct. **1225**, 129132 (2021)

Publisher's Note Springer Nature remains neutral with regard to jurisdictional claims in published maps and institutional affiliations.